

NEAR INFRARED SPECTROSCOPY OF THE TYPE II_n SN 2010jl: EVIDENCE FOR HIGH VELOCITY EJECTA

H. Jacob Borish¹, Chenliang Huang¹, Roger A. Chevalier¹, Benjamin M. Breslauer^{1,2},
Aaron M. Kingery^{1,3}, George C. Privon^{1,4}

ABSTRACT

The Type II_n supernova SN 2010jl was relatively nearby and luminous, allowing detailed studies of the near-infrared (NIR) emission. We present 1 – 2.4 μm spectroscopy over the age range of 36 – 565 days from the earliest detection of the supernova. On day 36, the H lines show an unresolved narrow emission component along with a symmetric broad component that can be modeled as the result of electron scattering by a thermal distribution of electrons. Over the next hundreds of days, the broad components of the H lines shift to the blue by 700 km s^{-1} , as is also observed in optical lines. The narrow lines do not show a shift, indicating they originate in a different region. He I $\lambda 10830$ and $\lambda 20587$ lines both show an asymmetric broad emission component, with a shoulder on the blue side that varies in prominence and velocity from -5500 km s^{-1} on day 108 to -4000 km s^{-1} on day 219. This component may be associated with the higher velocity flow indicated by X-ray observations of the supernova. The absence of the feature in the H lines suggests that this is from a He rich ejecta flow. The He I $\lambda 10830$ feature has a narrow P Cygni line, with absorption extending to $\sim 100 \text{ km s}^{-1}$ and strengthening over the first 200 days, and an emission component which weakens with time. At day 403, the continuum emission becomes dominated by a blackbody spectrum with a temperature of $\sim 1900 \text{ K}$, suggestive of dust emission.

Subject headings: circumstellar matter — supernovae: general — supernovae: individual (SN 2010jl)

¹Department of Astronomy, University of Virginia, P.O. Box 400325, Charlottesville, VA 22904-4325; hjborish@virginia.edu

²Google, 1600 Amphitheatre Pkwy, Mountain View, CA 94043

³ERC Incorporated/Jacobs ESSSA Group, NASA Marshall Space Flight Center, Huntsville, AL 35812

⁴Departamento de Astronomía, Universidad de Concepción, Casilla 160-C, Concepción, Chile

1. INTRODUCTION

Type IIn supernovae (SNe IIn) are characterized by narrow optical emission lines and a blue continuum (Schlegel 1990). The presence of a narrow line component at early times is taken to indicate a dense surrounding circumstellar medium that is heated and ionized by radiation from the explosion and the continuing interaction. The presence of wings on the narrow lines, as observed for the Type IIn SN 1998S (Leonard et al. 2000), can at least in some cases be explained by electron scattering in a mildly optically thick medium (Chugai 2001). The optical luminosity of a Type IIn event can also be explained by shock interaction with a dense circumstellar medium (Chugai & Danziger 1994). The velocity of the circumstellar mass loss can be deduced from the velocities indicated by P Cygni line profiles observed in the H Balmer lines; the typical line velocities are $100 - 1400 \text{ km s}^{-1}$ (Kiewe et al. 2012). The mass loss rates implied by the interaction luminosities are $\sim 0.01 - 0.1 M_{\odot} \text{ yr}^{-1}$. High mass loss rates were also derived from infrared emission attributed to circumstellar dust (Fox et al. 2011). Roughly 6% – 11% of core collapse supernovae are of Type IIn (Smith et al. 2011a).

These rates of mass loss are much higher than those found in normal stars, and the place of Type IIn events in stellar evolution is unclear. The progenitor stars have been linked to luminous blue variables (LBVs) because these have the requisite mass loss density and outflow velocity during their eruptive phases (e.g., Smith et al. 2010; Fox et al. 2011; Kiewe et al. 2012). In addition, the progenitor of SN 2005gl is consistent with an LBV (Gal-Yam & Leonard 2009). A problem is that stars in this evolutionary phase are not expected to undergo supernova explosions (although see the rotating models of Groh et al. 2013). Suggestions for the proximity in time of mass loss and explosion include wave-driven mass loss (Quataert & Shiode 2012) and binary-driven mass loss (Chevalier 2012), but these studies are very speculative. Soker (2013) also attributes the dense circumstellar medium around SNe IIn to binary interaction.

The bright Type IIn supernova SN 2010jl was discovered on UT 2010 November 3.5 by Newton & Puckett (2010). It was subsequently confirmed at an unfiltered magnitude of 12.9. Pre-discovery images showed that the supernova was present on 2010 October 9.6 (Stoll et al. 2011), which we use as our zero point in time. The supernova is located at R.A. = $9^{\text{h}}42^{\text{m}}53^{\text{s}}33$, Dec. = $+9^{\circ}29'41''.8$ (equinox 2000.0). It lies $2''.4$ east and $7''.7$ north of the center of the host galaxy, UGC 5189A. We take the distance to the supernova to be 49 Mpc (Smith et al. 2011b) and the reddening to be $E(B - V) = 0.058$ (Fransson et al. 2014). Smith et al. (2011b) used pre-explosion HST imaging to identify a bright, blue point source coincident with the position of the supernova, which they took to imply that the progenitor of SN 2010jl had a mass above $30 M_{\odot}$. Andrews et al. (2011) observed the supernova in the

Spitzer 3.6 and 4.5 μm bands and the *JHK* bands during days 90 – 108, finding evidence for 7500 K and 750 K components. However, Fransson et al. (2014) have examined the IR data for this age and find the temperature of the cool component to be ~ 1800 K; this temperature characterizes the cool component for 100’s of days. Fransson et al. (2014) presented one 0.3 – 2.4 μm spectrum of SN 2010jl (on day 460), as well as extensive optical and ultraviolet observations and near infrared (NIR) photometry. *Spitzer* observations were also presented by Fox et al. (2013), who find evidence for circumstellar emission and a high mass loss rate. Maeda et al. (2013) presented a spectrum (optical through NIR) on day 563, finding evidence for dust formation in the supernova ejecta.

SN 2010jl has also been detected as an X-ray source (Immler et al. 2010; Chandra et al. 2012; Ofek et al. 2014). Observations on 2010 December 7 – 8 (day 58 since discovery of the supernova) showed a hot ($kT > 8$ keV) thermal spectrum with an absorbing column $\sim 10^{24} \text{ cm}^{-2}$, assuming incomplete ionization of the circumstellar gas and a metallicity 0.3 of solar (Chandra et al. 2012). This column density corresponds to an electron scattering optical depth ~ 1 . By 2011 October 17 – 18 (day 372), the absorbing column declined by a factor of 3, but the X-ray emission remained steady and hot ($kT > 12$ keV). However, Ofek et al. (2014) re-examined the *Chandra* data and found them difficult to model. Hard X-ray observations with *NuSTAR* on 2012 October 6 yielded a temperature of $\sim 18_{-4}^{+6}$ keV (Ofek et al. 2014), which corresponds to a shock velocity of $\sim 4000 \text{ km s}^{-1}$.

Here we present a set of 10 NIR spectra of SN 2010jl spanning 529 days (Section 2). The various components contributing to the line and continuous emission are described in Section 3. The physical picture implied by the observations is discussed in Section 4 and the conclusions are in Section 5.

2. OBSERVATIONS

Data presented here were obtained using TripleSpec, an 0.9 – 2.4 μm , $R \sim 3000$ spectrograph, on the ARC 3.5 m telescope at Apache Point Observatory (Wilson et al. 2004; Herter et al. 2008). The supernova was observed 10 times between 2010 November 15 and 2012 April 26. Table 1 shows the details of each observation. Day numbers listed in Table 1 refer to time elapsed since the first detection of the supernova on 2010 Oct 9. Integration time refers to the total exposure time for each date. Individual exposures were 5 minutes in length and nodded in an ABBA pattern along the slit. We also observed the spectrophotometric standard HD 85377 for the telluric correction and photometric calibration. The airmass at the time of each observation is given in Table 1 for both SN 2010jl and HD 85377. Sky subtraction was achieved by differencing each pair of A and B exposures. Sky subtrac-

tion, spectral extraction, telluric correction, and photometric calibration were carried out using a modified version of the IDL utility *SpexTool* (Cushing et al. 2004).

Figures 1 – 3 show the spectra in the J , H , and K bands, respectively. The spectra are normalized to have the same continuum intensity at $1.55\ \mu\text{m}$. Identifications of the dominant lines are given.

Variations in seeing and cloud cover are problematic for photometric calibration of any long-slit spectrum. Therefore, the photometric calibrations produced by *SpexTool* are only roughly accurate. Much of the following discussion deals with descriptions of the line or continuum shapes, rendering a precise photometric calibration unimportant. Figures 5, 9, 15, and 16 show the true flux density as revealed by photometric observations collected by Fransson et al. (2014). To estimate H -band magnitudes at the exact dates of our observations we fit separate 2^{nd} degree polynomials to the early time (before 250 days) and late time (after 403 days) H -band light curves published by Fransson et al. (2014). Because Fransson et al. (2014) does not publish photometry nearby in time to day 403, we used cubic spline interpolation over the full light curve to estimate the magnitude at 403 days. As a result, the calibration to the photometry for day 403 is somewhat more uncertain than that at other dates. Nevertheless, the behavior of the flux density at day 403 seems to fall in line with the other observations. Once H magnitudes had been determined for each TripleSpec observation, we converted each magnitude to a flux density using

$$H = -2.5 \log(f_{1.63\mu\text{m}}) - 24.860, \quad (1)$$

where $1.63\ \mu\text{m}$ and -24.860 are the effective wavelength and magnitude zero-point of the NIR H -band as given by Bessell et al. (1998). We then scaled the spectra output by *SpexTool* to the level of the calculated flux density at $1.63\ \mu\text{m}$.

3. SPECTRAL COMPONENTS

3.1. Continuum Emission

At early times the continuum emission has a slope that is slightly flatter than Rayleigh-Jeans. The flatness of the continuum relative to the blackbody shape indicates the combination of warm and cool components. The reason for this can be seen in the decomposition of the continuum emission by Fransson et al. (2014), who model the optical through infrared spectrum and find that a relatively cool ($1800 - 1900\ \text{K}$) component is present from early times as well as a warmer ($\sim 7000\ \text{K}$) component. Because the blackbody peak is in the optical range, temperatures determined from optical observations should be more reliable

than those determined from the infrared through day 219. At times in excess of one year, the continuum emission has a local maximum within the wavelength range of our observations. On 2011 November 17 (403 days), the continuum peak is found at about $1.5\ \mu\text{m}$. By 2012 February 9 (488 days), it has moved to about $1.7\ \mu\text{m}$. Figure 4 presents the spectrum at 488 days overlaid with five blackbodies ranging in temperature from 1500 to 1900 K, showing that the observed continuum is flatter than a blackbody. Modifying the blackbody curve to account for the emissivities of various dust grains does not produce a shape which fits the continuum emission because the efficiency of dust emission drops with increasing wavelength.

Assuming a cooler component contributes to the emission at wavelengths longer than $1.5\ \mu\text{m}$, we identified selected areas of continuum emission and fit to a blackbody using the IDL fitting package MPFIT (Markwardt 2009; Moré 1978) for each observation later than 1 year. The temperatures of these fits are $\sim 2000\ \text{K}$ and are shown in Table 2. In Figure 4, the best fits to the continuum short of $1.9\ \mu\text{m}$ lie well within 100 K of 1800 K. We therefore cite an approximate uncertainty of $\pm 75\ \text{K}$ for these temperatures. This is the uncertainty in the shortest wavelength emission observed in the NIR and does not take into account the evidence for cooler emission at wavelengths longer than $1.9\ \mu\text{m}$. By fitting the shortest wavelength emission we estimate the temperature of the warmest dust. Although the shape of the continuum on days 488 and 565 does not fit a pure blackbody, a temperature of $\sim 1900 - 2000\ \text{K}$ is consistent with emission from hot dust and with the observations of Fransson et al. (2014). Such emission has previously been observed in a number of Type II supernovae (Fox et al. 2011).

3.2. Hydrogen Lines

As can be seen in Figures 1 – 3, many emission lines of the Paschen and Brackett series of H are detected. Each line shows 2 distinct components: a narrow component that is close to zero velocity in the host galaxy and a broad component. Although narrow lines could have their origin in the interstellar medium of the host galaxy, we attribute the emission primarily to the unshocked circumstellar medium. One reason is that the fluxes of narrow lines at later times ($t \gtrsim 380\ \text{day}$) decline to about 1/10 of the fluxes at earlier times, implying we can comfortably ignore the contribution of host galaxy emission lines at early times. Another reason is that interstellar emission lines would also be present in the Balmer series. Observations of the early $\text{H}\alpha$ line show a narrow P Cygni feature (Smith et al. 2011b; Fransson et al. 2014), indicating that the circumstellar medium is optically thick in the H Balmer lines. The P Cygni features observed in the $\text{H}\alpha$ line indicate an expansion velocity of $100\ \text{km s}^{-1}$ (Fransson et al. 2014). The Paschen and Brackett series lines do not show

absorption, suggesting they are optically thin. The narrow lines are plausibly formed in a region of circumstellar mass loss.

Broadened emission from hydrogen is visible in the data throughout the accessible lines of the Paschen and Brackett series. The best detected lines are Paschen β , Brackett γ , and Paschen δ . The shape and evolution of the Paschen β line are shown in Figure 5. Paschen γ is also strong, but is heavily blended with the red side of the broad He I $\lambda 10830$ line. Paschen ϵ is sometimes observed, but it lies on the edge of an atmospheric absorption region, making the determination of its shape and strength strongly dependent on changing atmospheric conditions. Many of the weaker Brackett series lines are identifiable in the data, and corroborate the common line shape of broad H emission.

At early times, the broad component is fairly symmetric about zero velocity. In other Type II supernovae, a Lorentzian profile gives a reasonable fit to broad Balmer lines (Leonard et al. 2000; Smith et al. 2010). Here, the broad Paschen β line is moderately well fit by a Lorentzian profile (see also Smith et al. 2011b, for H α). However, the broad line profile is presumably the result of the thermal particle velocities and scattering; this situation does not naturally produce a Lorentzian profile. The broad line profile is naturally produced by electron scattering (Chugai 2001; Fransson et al. 2014), without the need for Doppler effects due to bulk motion. The narrow line component is made up of photons that escape without scattering, so its strength relative to the broad component places constraints on the scattering optical depth to the line photon source. At early times, the broad component is symmetric, implying that the electron thermal velocities are much larger than systematic velocities. At late times, the broad lines are seen to become asymmetric with regard to zero velocity, although the H α line remains fairly symmetric relative to the line peak (Fransson et al. 2014); the peak of the broad component shifts to the blue by $\sim 700 \text{ km s}^{-1}$, as also occurs in the optical lines. Figure 5 shows that the extended wings in the Paschen β line have diminished by day 400. We take this to indicate that the electron scattering optical depth is decreasing, which could occur because the shock wave overruns the scattering region or there is a change in the ionization of the gas.

In addition to finding that the emission lines shift to the blue with time, Fransson et al. (2014) found that the lines remain symmetric about a blueshifted wavelength during the shift. They used this property to argue that the line emission and scattering occur in a comoving slab of material. In Figure 6 we show the Paschen β line on day 219 as well as its reflection about a particular velocity, using a procedure essentially the same as that used by Fransson et al. (2014). The velocity of the shift is chosen so that the wings of the lines over $1000 - 5000 \text{ km s}^{-1}$ match up. It can be seen that there is an asymmetry near the peak of the line. Although the asymmetry is small, it shows that the hypothesis of electron

scattering in a comoving slab is not completely accurate. Fransson et al. (2014) presented NIR spectroscopy of the supernova on day 465, finding symmetry of the lines at that time. Our late time spectra also show that the degree of asymmetry becomes small.

Figure 7 compares the broad components of the Paschen β , Brackett γ , and Paschen δ lines at one time, 164 days. It can be seen that the FWHM of the lines are similar. There are deviations in the line wings, but this aspect is sensitive to the continuum subtraction. We conclude that there is no strong evidence for differences between the lines. In the case of SN 1994W, Dessart et al. (2009) discussed differences between these lines caused by differences in optical depth. However, those authors were considering a case where the emission was from shocked, and thus very high density, gas. In our case, we believe the broad lines are formed in the unshocked circumstellar medium, where the densities are lower.

Figure 8 and Table 3 shows the evolution of the flux in the narrow component to that in the broad component of Paschen β , Paschen δ , Brackett γ , and OI $\lambda 11287$. Figure 8 and Table 4 show the evolution of the equivalent widths of the prominent lines. In order to measure both narrow component strength to broad component strength ratios and equivalent widths, a linear fit to the continuum in the vicinity of each emission line was found. The ratios of narrow component strength to broad component strength were measured by direct integration over each component after subtraction of the continuum fit. The quoted uncertainties were found by allowing the full width of the narrow component to vary by one pixel in each direction while also taking into account the noise in the continuum about the line. It can be seen that the ratio of narrow to broad line flux decreases with time. Equivalent widths were measured by directly integrating over the ratio of line to continuum. The quoted uncertainties were found by allowing the constant parameter in the linear continuum fit to vary by 1σ in both directions. There is an initial approximately linear increase of the equivalent width with time, followed by a decline between days 220 and 400. Zhang et al. (2012) and Fransson et al. (2014) found a similar evolution for the $H\alpha$ line.

3.3. He lines

Broad He emission features are detected at $1.0830\mu\text{m}$ and $2.0587\mu\text{m}$. The evolution of the He lines, especially He I $\lambda 10830$, shows some similarities to the H lines, although there are significant differences (Figure 9). The broad component shows an increasing equivalent width, in the same way as the H lines (Figure 8). A comparison of the He I $\lambda 10830$ line with the Paschen β line on day 164 is shown in Figure 10. It can be seen that both lines show extended wings going out $\sim 8000 - 9000 \text{ km s}^{-1}$. On the red side of the He I $\lambda 10830$ line, there is the superposition of the Paschen γ line, which has both broad and narrow emission

components like the Paschen β line. Assuming the line profile of Paschen γ is identical to Paschen β , in Figure 10 we use Paschen β as a template to obtain a Paschen γ subtracted He profile. The shift and scale of the Paschen β template is chosen in order to best fit the template narrow peak to the narrow peak of Paschen γ . The peak of the broad component shows a shift to the blue by $\sim 1000 \text{ km s}^{-1}$ in contrast to the $\sim 700 \text{ km s}^{-1}$ shift in the peak of the H lines (Figure 10 inset). As described below, we attribute this difference to an additional component in the He line.

On the blue side on day 164, there is a shoulder feature in the He I line that is not present in the H line. In Figure 10, the Paschen γ -subtracted He I line is overplotted with the Paschen β line so that the line profiles match at positive velocities. We have used a similar procedure to search for excess emission on the other dates of observation. On days 36 and 53, the feature is not discernable; on days 402 and 488, there is not a well defined shoulder feature, but there is weak excess He emission that peaks at $\sim -2500 \text{ km s}^{-1}$. The feature grows and fades in relative strength roughly in the same way as the broad H lines. One possibility for the origin of this feature is that it is a separate line with only a broad component and no narrow component. However, a comparison of the He I $\lambda 10830$ line to the He I $\lambda 20587$ line (Figure 11) shows that the shoulder feature is present in both lines. The broad wings are likely due to electron scattering; components with different temperatures are possible, but this would not produce a shoulder structure on one side of the line profile. The implication is that the feature is due to material with systematic velocities up to $\sim 5000 \text{ km s}^{-1}$ towards the observer. Figure 12 shows the excess blueshifted emission in the He I $\lambda 10830$ line relative to the Paschen β line; the emission extends to at least -6000 km s^{-1} . In addition, the shoulder feature of excess emission moves to the red with time (Figure 13), which is the opposite of the evolution of the H broad features. The deceleration of the break in the shoulder feature follows a velocity evolution $t^{-0.39 \pm 0.08}$ (Figure 14). The error bars in the shoulder-break velocities shown in figure 14 are estimated by measuring the overlap of the 1σ uncertainty regions for each linear fit component shown in figure 12.

In addition to the broad line feature, there is a narrow P Cygni feature in the He I $\lambda 10830$ line. Figure 15 shows that initially (day 36) the emission component dominates over the narrow absorption. By day 53, the 2 components are at nearly equal strength and at later times, the absorption component dominates. Since the resolution of the observations is about 100 km s^{-1} , we place an upper limit of 100 km s^{-1} on the wind velocity of the CSM. The width of the absorption line does not change with the time of our observations. The same is true for the H α line (Fransson et al. 2014). This is indicative of the formation of the circumstellar medium in an approximately steady flow. If the material were launched in an eruptive event, the CSM velocity would increase roughly linearly with radius, and over time

the observed emission-line widths should increase. This is not observed, at least within the spectral resolution. The narrow component in the He I $\lambda 20587$ line is not as well defined as in the $\lambda 10830$ line; it appears only in absorption.

3.4. Other Lines

The O I line at $1.129 \mu\text{m}$ is in a noisy part of the spectrum where there is confusion with night sky features. In addition, it overlaps the red wing of the He I $\lambda 10830$ line, but it is clearly present (Figure 16). The line shows a broad emission component with properties and an evolution that are comparable to those of the H lines. A narrow line may be detected but is uncertain because of the contamination by night sky lines. The observed emission is compatible with the view that the O I line is the result of pumping by the $\text{Ly}\beta$ line (Fransson et al. 2014).

In addition, there is a line present at $\sim 1.2 \mu\text{m}$ (Figure 16). It has a broad, but no narrow, component. We tentatively identify it as Si I $1.1991 - 1.2270 \mu\text{m}$. We also considered Mg I $\lambda 11828$, but it gave a poor fit to the line profile, under the assumption that the line profile is comparable to that of He I $\lambda 10830$. The line profile, when taken to be the Si I line, shows that there is emission associated with the blue shoulder emission observed in the He lines (Figure 17).

4. PHYSICAL PICTURE

Our interpretation of the NIR spectra builds on previous discussions of Type II_n supernovae (Chugai & Danziger 1994; Leonard et al. 2000; Fransson et al. 2002; Hoffman et al. 2008; Fransson et al. 2014). One component is the pre-supernova mass loss region with which the supernova is interacting. The mass loss has an outward velocity of 100 km s^{-1} and is fairly steady over the region of observation. The region is photoionized by X-ray radiation coming from the shock interactions.

In our first epoch of NIR spectra, the H line profiles show a narrow component due to the slow wind and a broad symmetric component that we attribute to electron scattering in the slow wind. The line width reflects a combination of the electron scattering optical depth, τ_e , and the gas temperature (Chugai 2001; Huang et al. 2014). We initially assume that the emitting gas is the same as the scattering gas, and both are associated with the slow wind which has a density profile $n \propto r^{-2}$ over an extended region. The scattering process was modeled by a Monte Carlo code to follow the scattering and wavelength shifts of line

photons. As in Fransson et al. (2014), the broad line component is well-reproduced by the electron scattering line profile (Figure 18). The model assumed spherical symmetry, with an absorbing sphere for an inner boundary R_i . As shown in Huang et al. (2014), the FWHM of the scattered line, which has an approximately exponential shape, depends on the optical depth to R_i , τ_e , and the temperature T . Provided that the ratio of outer radius to R_i is > 10 , the results are not sensitive to the exact value of the ratio. The line width in velocity space is proportional to the thermal velocity and is thus $\propto T^{1/2}$. For the Paschen β line on day 36 we find the observed FWHM to be $\sim 2030 \text{ km s}^{-1}$, which is consistent with the following pairs of values of (τ_e, T) : (1, 58600 K), (5, 16400 K), (10, 7760 K), and (20, 3700 K).

After interpolating over the narrow component of the day 36 Paschen β line, we perform least squares fits of the electron scattering models to the broad component. We find the reduced χ^2 to lie in the range $1.39 - 1.55$ for τ_e ranging between 20 and 1 (Figures 18). The data is best fit to the $\tau_e = 20$ profile, with a reduced χ^2 of 1.39. Such a high optical depth should be viewed with skepticism, especially in view of the small range of χ^2 when τ_e varies between 1 and 20.

If the emitting and scattering gas are the same, another constraint on the emission comes from the ratio of the narrow line flux to the flux in the broad wings, which is found to be 0.17 on day 36 for the Paschen β line. Using the model results from Huang et al. (2014), we find that the ratio observed for SN 2010jl corresponds to $\tau_e \sim 4$, which suggests a lower limit of the scattering gas optical depth by assuming there is no other source of narrow line emission. The observed temperature is then $\sim 20,000 \text{ K}$, which is reasonable for the ionized gas. Another measure of τ_e is provided by the outer wings of the line. By adjusting the temperature, we can generate line profiles with the same FWHM at different τ_e , the line wings become slightly stronger for higher values of τ_e . However, our data for SN 2010jl do not have sufficient signal-to-noise in the wings to be able to use this method (Figure 18), as is indicated by the small range of reduced χ^2 over the range of τ_e from 1 to 20.

Although a consistent picture for mixed emission and scattering can be developed for the earliest time, it has problems at later times, indicating that application of the model to the narrow line at early times may be misleading. Over 100's of days, the broad component in the lines shifts to the blue, as also observed in optical lines (Fransson et al. 2014). One suggestion is that the shift is due to dust formation in the expanding medium (Smith et al. 2012; Maeda et al. 2013; Gall et al. 2014). In that picture, the redshifted photons emitted by material expanding away from the observer on the far side of the supernova are preferentially absorbed as they travel through a longer column of dust than their blueshifted near side counterparts. This would lead to a line profile that is less strong on the red side, an effect

that would be more pronounced in the shorter wavelength lines as dust absorption within the ultraviolet/optical/near-infrared bands is more effective at shorter wavelengths. Smith et al. (2012) made this argument based on spectra at an age ~ 100 days and Maeda et al. (2013) based on a spectrum at age 563 days. At the earlier times, our spectra show a shift in the Brackett γ line that is similar to that at shorter wavelengths (Figure 7), although there is some uncertainty in the continuum level. However, our observations cover a relatively small, long wavelength range and do not provide a good test of wavelength dependent line profiles.

Fransson et al. (2014) discussed a number of problems with the shift in the broad component being due to dust, and proposed a model in which there is radiative acceleration of the gas that gives rise to the broad component. Since the narrow component does not shift to the blue along with the broad component, the two components must originate in different places. The equivalent width in the narrow component of the H lines remains roughly constant over the first 200 days, so the ionized circumstellar medium appears to evolve slowly and the growth in the equivalent width of the H lines is primarily due to the growth of the broad component. Over the first 200 days, the NIR luminosity of SN 2010jl dropped by a factor of 3 (Fransson et al. 2014), so the narrow lines dropped by this factor and the flux in the broad components approximately doubled from our earliest observation to an age of 200 days. Formation of the narrow and broad lines in the same place would imply that the optical depth increases with time because fewer photons escape without scattering at higher optical depth. This is unexpected, giving further evidence that the line components form in separate regions. The properties of the H emitting regions are distinct from those of the X-ray emitting region, where the shock front has a velocity $\sim 4000 \text{ km s}^{-1}$ and a preshock $\tau_e \sim 1$ on day 58 if there is incomplete ionization of the gas (Chandra et al. 2012; Ofek et al. 2014). The preshock column density subsequently declines. As discussed by Fransson et al. (2014), the fact that the broad component shows a systematic shift indicates that there is a large scale asymmetry in the object and that the optical emission is perhaps from a polar flow.

As discussed in Section 2.3, the NIR He lines show a difference with the H lines. In addition to the growth of a broad component shifted by -1000 km s^{-1} , the He lines develop a shoulder out to -4000 to -5500 km s^{-1} . The velocity indicates that this component may be associated with the higher velocities inferred from the X-ray emission. The fact that this feature does not appear in the H lines indicates a difference in composition; the high velocity He feature may be associated with supernova ejecta in which H is underabundant.

A surprisingly similar situation has been observed in the Type IIn SN 1997eg (Hoffman et al. 2008). SN 1997eg had a maximum absolute V magnitude ~ 1.5 magnitudes fainter than SN 2010jl, so a lower density interaction is indicated. Hoffman et al. (2008) find that the H

lines do not have Lorentzian profiles, implying that electron scattering related to the thermal velocities of electrons is not important and consistent with a low density. In addition, SN 1997eg was detected as a radio source at an age of 7 months (Lacey et al. 1998). No detections of SN 2010jl have yet been reported, suggesting higher absorption in this case. Despite the apparent difference in circumstellar density, there are interesting similarities in the H and He lines. In SN 1997eg, the H Balmer lines showed a shift in the peak of the line to the blue by $\sim 700 - 800 \text{ km s}^{-1}$. At the same time, the He I $\lambda 7065$ and $\lambda 5876$ lines showed a strong shoulder of emission to the blue by $\sim 5000 \text{ km s}^{-1}$. At later times, a peak like the one extending to the blue developed to the red in the H lines. Hoffman et al. (2008) interpret the line emission as coming from an asymmetric region with different geometries for the H and He dominated emission regions. The H lines are attributed to shocks driven into a dense circumstellar disk or torus, while the He emission is from H depleted gas that is expanding more rapidly into a lower density circumstellar medium. This view is supported by polarization observations of the supernova.

Our observations of H and He lines in SN 2010jl show similar shifts. The H lines show only a blueshifted component, without the redshifted side. We attribute the difference to the higher density and optical depths in the SN 2010jl case. There is also evidence for blueshifted He rich gas moving at 5000 km s^{-1} . However, the He emission is also strong in the lower velocity component, as opposed to the case of SN 1997eg.

Our spectral line observations indicate 3 kinds of emitting regions: a narrow line region of presupernova mass loss with velocities $\sim 100 \text{ km s}^{-1}$, an intermediate line region involving $\sim 700 \text{ km s}^{-1}$ gas in an asymmetric structure, and **a He dominant region of supernova ejecta with velocities $\sim 5000 \text{ km s}^{-1}$. The lines are affected by electron scattering in the early phases of evolution and electron scattering may be responsible for the extended line wings through day ~ 400 . After day 400, the lines no longer show the characteristic electron scattering profiles and the line widths probably reflect gas velocities to $\sim 2000 \text{ km s}^{-1}$. However, the bulk of H rich material is moving at $\sim 700 \text{ km s}^{-1}$. The broad feature observed in the He lines could be produced by a uniformly expanding shell of gas with velocity $\sim 5000 \text{ km s}^{-1}$; the absence of the redshifted part of the shell may be due to the supernova being opaque.** Similar regions have been observed in other Type II_n supernovae, although the high velocity ejecta region is sometimes observed to be O rich, e.g., SN 1986J (Milisavljevic et al. 2008) and SN 1995N (Fransson et al. 2002).

5. DISCUSSION AND CONCLUSIONS

Our study shows that NIR spectral observations of Type IIn supernovae can provide an interesting window on these events. For the H lines in SN 2010jl at early times, the NIR lines (Brackett and Paschen series) have broad components with profiles that are similar to the broad components of the optical Balmer lines (Zhang et al. 2012; Fransson et al. 2014). The line profiles are consistent with the lines being formed by electron scattering in the circumstellar medium. The narrow line components in the Balmer lines show absorption features, i.e. they are optically thick, while the Paschen and Brackett lines are not. The NIR narrow emission thus gives a measure of the flux of unscattered line photons emitted by the slow circumstellar medium.

In SN 2010jl, the optical He I lines are relatively weak so there is not much information on their profiles. However, the NIR $\lambda 10830$ line is strong and the profile is well defined in our observations. We find a clear difference with the H lines in that there is a shoulder to the blue that implies gas approaching at $4000 - 5500 \text{ km s}^{-1}$. The emission can be interpreted as H poor supernova ejecta that are expanding into a region of relatively small circumstellar density. A similar situation is observed in SN 1997eg (Hoffman et al. 2008).

The NIR continuum can provide important information on the emission from warm dust, which appears to be frequently present around Type IIn supernovae (Fox et al. 2011). However, at early times the hotter photospheric emission is present and optical observations are needed to separate out the photospheric emission from the dust emission (Fransson et al. 2014). At later times, when the photospheric emission has faded, the NIR observations can provide crucial information on dust emission.

We are grateful to Ori Fox for help with the observations as well as discussion of the results. We thank Claes Fransson for fruitful discussions and correspondence on SN 2010jl, and the referee who provided detailed comments that led to significant improvement of the paper. Thanks are also due to Meredith Drosback, Sarah Schmidt, and Yue Shen, who very graciously donated telescope time for our observations of SN 2010jl. We also wish to thank Mike Skrutskie for his help with gathering, reducing, and interpreting the spectra. This research was supported in part by NSF grant AST-0807727 and NASA grant NNX12AF90G. The research has made use of the SIMBAD database, operated at CDS, Strasbourg, France, and the NASA/IPAC Extragalactic Database (NED) which is operated by the Jet Propulsion Laboratory, California Institute of Technology, under contract with the National Aeronautics and Space Administration.

Facilities: APO (TripleSpec).

REFERENCES

- Andrews, J. E., Clayton, G. C., Wesson, R., et al. 2011, *AJ*, 142, 45
- Bessell, M. S., Castelli, F., & Plez, B. 1998, *A&A*, 333, 231
- Chandra, P., Chevalier, R. A., Irwin, C. M., et al. 2012, *ApJ*, 750, L2
- Chevalier, R. A. 2012, *ApJ*, 752, L2
- Chugai, N. N. 2001, *MNRAS*, 326, 1448
- Chugai, N. N., & Danziger, I. J. 1994, *MNRAS*, 268, 173
- Cushing, M. C., Vacca, W. D., & Rayner, J. T. 2004, *PASP*, 116, 362
- Dessart, L., Hillier, D. J., Gezari, S., Basa, S., & Matheson, T. 2009, *MNRAS*, 394, 21
- Fox, O. D., Chevalier, R. A., Skrutskie, M. F., et al. 2011, *ApJ*, 741, 7
- Fox, O. D., Filippenko, A. V., Skrutskie, M. F., et al. 2013, *AJ*, 146, 2
- Fransson, C., Chevalier, R. A., Filippenko, A. V., et al. 2002, *ApJ*, 572, 350
- Fransson, C., Ergon, M., Challis, P. J., et al. 2014, *ApJ*, 797, 118
- Gal-Yam, A., & Leonard, D. C. 2009, *Nature*, 458, 865
- Gall, C., Hjorth, J., Watson, D., et al. 2014, *Nature*, 511, 326
- Groh, J. H., Meynet, G., & Ekström, S. 2013, *A&A*, 550, L7
- Herter, T. L., et al. 2008, *Ground-based and Airborne Instrumentation for Astronomy II*. Edited by McLean, 7014, 30
- Hoffman, J. L., Leonard, D. C., Chornock, R., et al. 2008, *ApJ*, 688, 1186
- Huang, C., et al. 2014, in preparation
- Immler, S., Milne, P., & Pooley, D. 2010, *The Astronomer’s Telegram*, 3012, 1
- Kiewe, M., Gal-Yam, A., Arcavi, I., et al. 2012, *ApJ*, 744, 10
- Lacey, C. K., Weiler, K. W., Sramek, R. A., & van Dyk, S. D. 1998, *IAU Circ.*, 7068, 2
- Leonard, D. C., Filippenko, A. V., Barth, A. J., & Matheson, T. 2000, *ApJ*, 536, 239

- Markwardt, C. B. 2009, *Astronomical Data Analysis Software and Systems XVIII*, 411, 251
- Maeda, K., Nozawa, T., Sahu, D. K., et al. 2013, *ApJ*, 776, 5
- Milisavljevic, D., Fesen, R. A., Leibundgut, B., & Kirshner, R. P. 2008, *ApJ*, 684, 1170
- Moré, J. 1978, *Numerical Analysis*, 630, 105
- Newton, J. & Puckett, T. 2010, *CBET*, 2532, 1
- Ofek, E. O., Zoglauer, A., Boggs, S. E., et al. 2014, *ApJ*, 781, 42
- Patat, F., Taubenberger, S., Benetti, S., Pastorello, A., & Harutyunyan, A. 2011, *A&A*, 527, L6
- Quataert, E., & Shiode, J. 2012, *MNRAS*, 423, L92
- Schlegel, E. M. 1990, *MNRAS*, 244, 269
- Smith, N., Chornock, R., Silverman, J. M., Filippenko, A. V., & Foley, R. J. 2010, *ApJ*, 709, 856
- Smith, N., Li, W., Filippenko, A. V., & Chornock, R. 2011a, *MNRAS*, 412, 1522
- Smith, N., Li, W., Miller, A. A., et al. 2011b, *ApJ*, 732, 63
- Smith, N., Silverman, J. M., Filippenko, A. V., et al. 2012, *AJ*, 143, 17
- Soker, N. 2013, preprint (arXiv:1302.5037)
- Stoll, R., Prieto, J. L., Stanek, K. Z., et al. 2011, *ApJ*, 730, 34
- Wilson, J. C., et al. 2004, *Ground-based Instrumentation for Astronomy*. Edited by Alan F. M. Moorwood and Iye Masanori. *Proceedings of SPIE*, 5492, 1295
- Zhang, T., Wang, X., Wu, C., et al. 2012, *AJ*, 144, 131

Table 1. Observing Details

Observation Date	Supernova Age (days)	Integration Time (minutes)	SN2010jl Airmass	HD85377 Airmass	Observers
2010 Nov 15	36	20	1.10	1.15	M. Drosback, O. Fox
2010 Dec 02	53	20	1.10	1.16	Y. Shen, O. Fox
2011 Jan 26	108	25	1.10	1.16	G. Privon, O. Fox
2011 Feb 22	135	20	1.10	1.18	Y. Shen, O. Fox
2011 Mar 23	164	20	1.32	1.47	S. Schmidt, O. Fox
2011 Apr 06	178	20	1.13	1.17	J. Borish, M. Skrutskie
2011 May 17	219	20	1.56	1.80	J. Borish, O. Fox
2011 Nov 17	403	40	1.59	1.50	J. Borish, B. Breslauer, A. Kingery
2012 Feb 09	488	40	1.14	1.24	J. Borish
2012 Apr 26	565	40	2.0	2.1	J. Borish

Table 2. Blackbody Fits to the Near Infrared

Observation Date	Supernova Age (days)	Blackbody Temperature (K)
2011 Nov 17	403	2090
2012 Feb 09	488	1890
2012 Apr 26	565	1910

Note. — Uncertainty in each temperature is approximately ± 75 K.

Table 3. Narrow to Broad Line Ratio

Date	Day	Paschen β	Paschen δ	Brackett γ
2010 Nov 15	36	0.20 \pm 0.028	0.12 \pm 0.021	0.16 \pm 0.029
2010 Dec 02	53	0.15 \pm 0.023	0.08 \pm 0.019	0.17 \pm 0.028
2011 Jan 26	108	0.07 \pm 0.017	0.05 \pm 0.017	0.08 \pm 0.023
2011 Feb 22	135	0.05 \pm 0.017	0.03 \pm 0.016	0.06 \pm 0.021
2011 Mar 23	164	0.05 \pm 0.017	0.03 \pm 0.016	0.05 \pm 0.020
2011 Apr 06	178	0.04 \pm 0.017	0.03 \pm 0.017	0.05 \pm 0.020
2011 May 17	219	0.03 \pm 0.017	0.03 \pm 0.016	0.04 \pm 0.020
2011 Nov 17	403	0.02 \pm 0.023	0.02 \pm 0.026	0.03 \pm 0.026
2012 Feb 09	488	0.04 \pm 0.027	0.04 \pm 0.033	0.06 \pm 0.029
2012 Apr 26	565	0.11 \pm 0.032

Table 4. Equivalent Widths (Angstroms)

Date	Day	Paschen β	Paschen δ	Brackett γ
2010 Nov 15	36	84 \pm 20	25 \pm 8	50 \pm 17
2010 Dec 02	53	114 \pm 16	36 \pm 7	59 \pm 12
2011 Jan 26	108	291 \pm 38	75 \pm 18	119 \pm 32
2011 Feb 22	135	371 \pm 34	93 \pm 17	160 \pm 24
2011 Mar 23	164	441 \pm 38	111 \pm 20	207 \pm 37
2011 Apr 06	178	480 \pm 48	118 \pm 22	219 \pm 39
2011 May 17	219	573 \pm 58	148 \pm 26	261 \pm 60
2011 Nov 17	403	156 \pm 11	64 \pm 20	29 \pm 5
2012 Feb 09	488	93 \pm 11	41 \pm 15	12 \pm 4
2012 Apr 26	565	71 \pm 29

Note. — **Broad and narrow line fluxes are included**

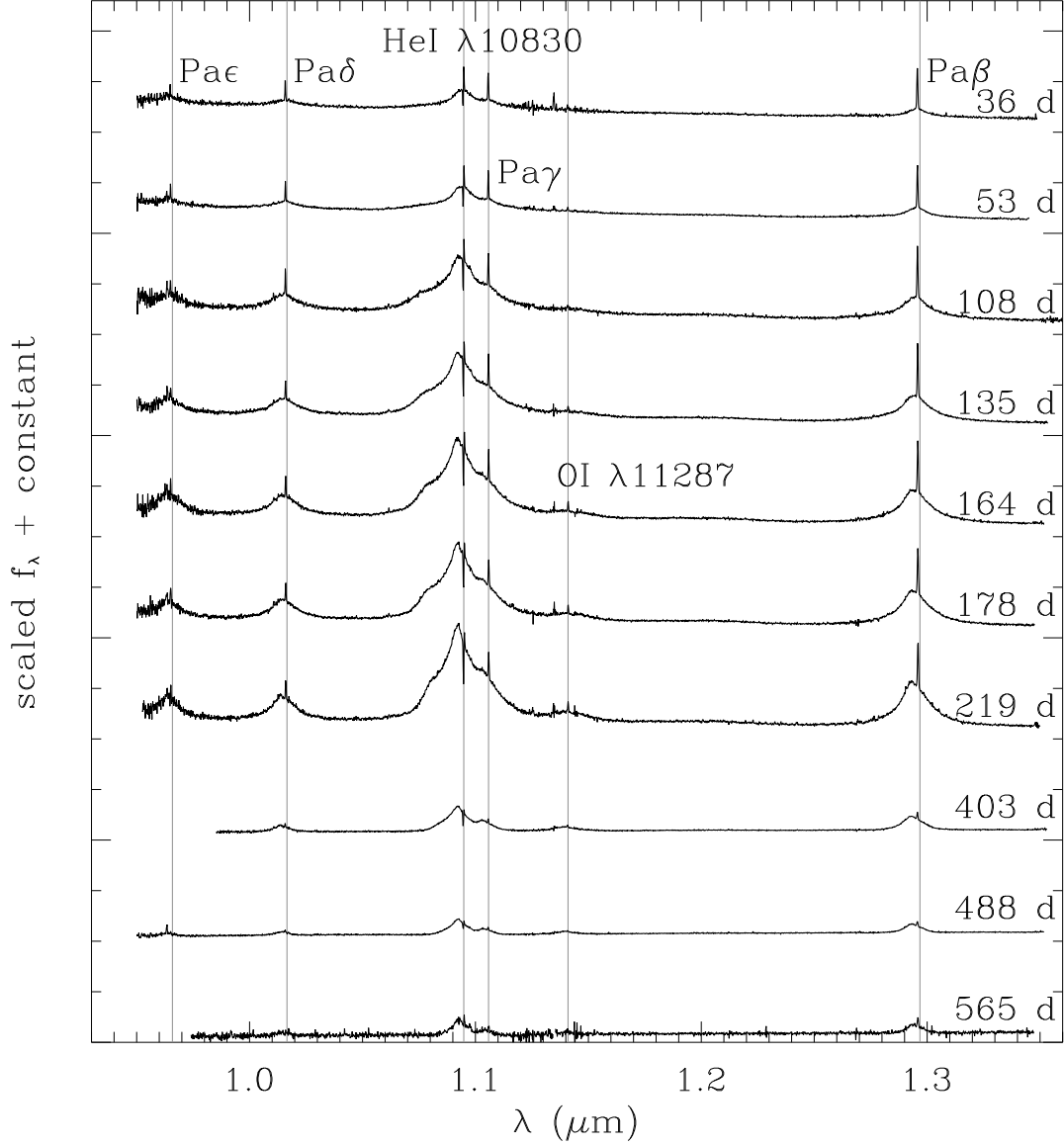


Fig. 1.— *J* band spectra of SN 2010jl taken at the ARC 3.5m Telescope. The data have not been corrected for redshift or reddening. The spectra have been scaled so that the continuum of each spectrum has the same strength at 1.55 μm and then displaced vertically for clarity. The day numbers refer to the earliest observation, 2010 October 9. Figures 2 and 3 were prepared in the same way.

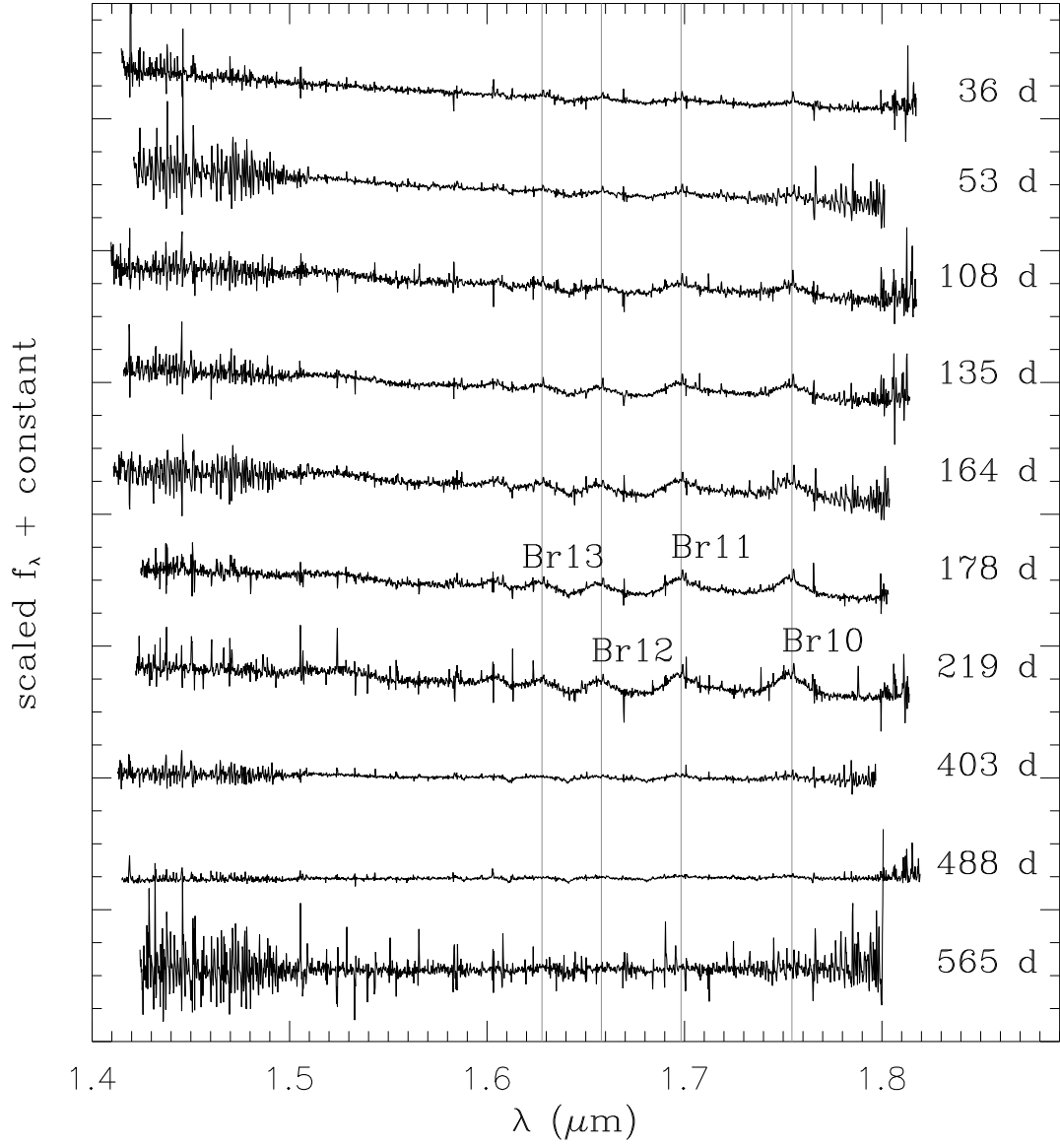


Fig. 2.— H band spectra of SN 2010jl taken at the ARC 3.5m Telescope.

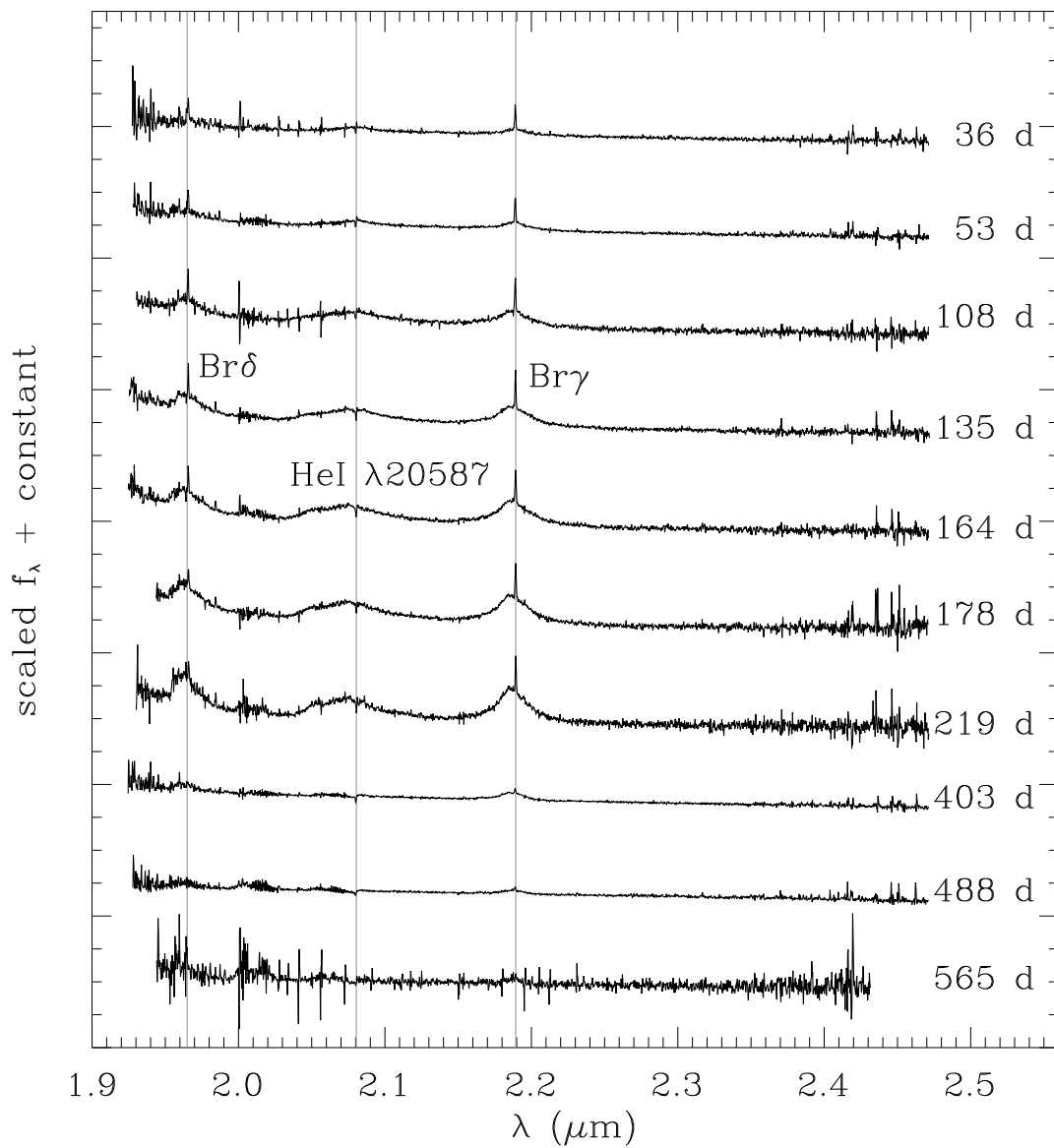


Fig. 3.— K band spectra of SN 2010jl taken at the ARC 3.5m Telescope.

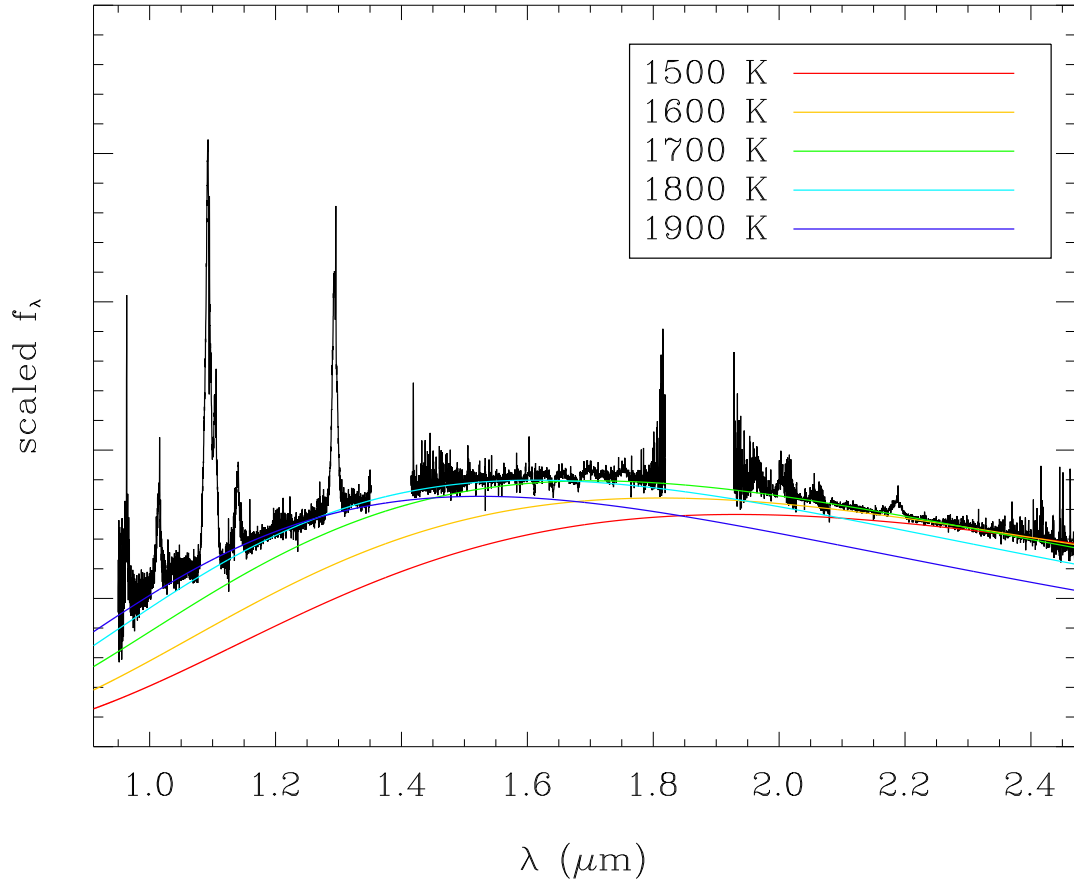


Fig. 4.— The spectrum at 488 days overlaid with blackbody curves. The blackbodies span the range in temperature for which the blackbody peak lies within the near-infrared.

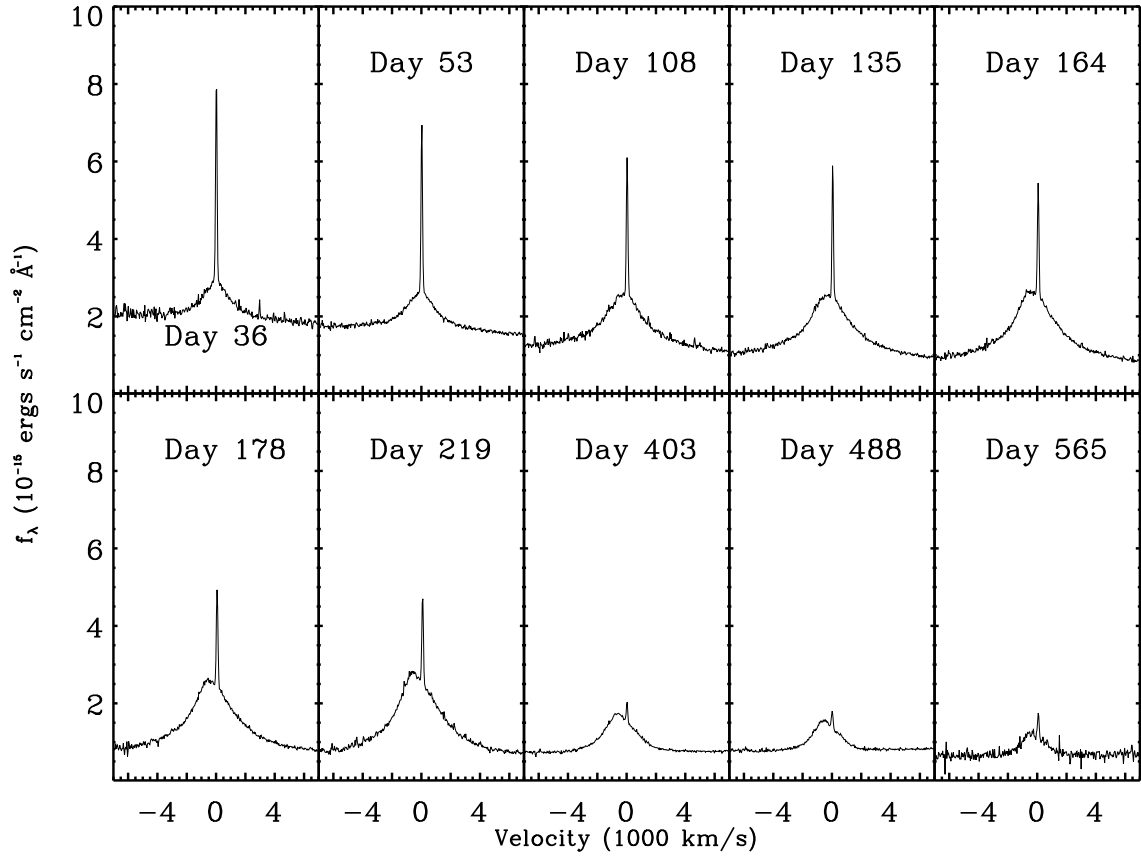


Fig. 5.— Time evolution of the Paschen β line.

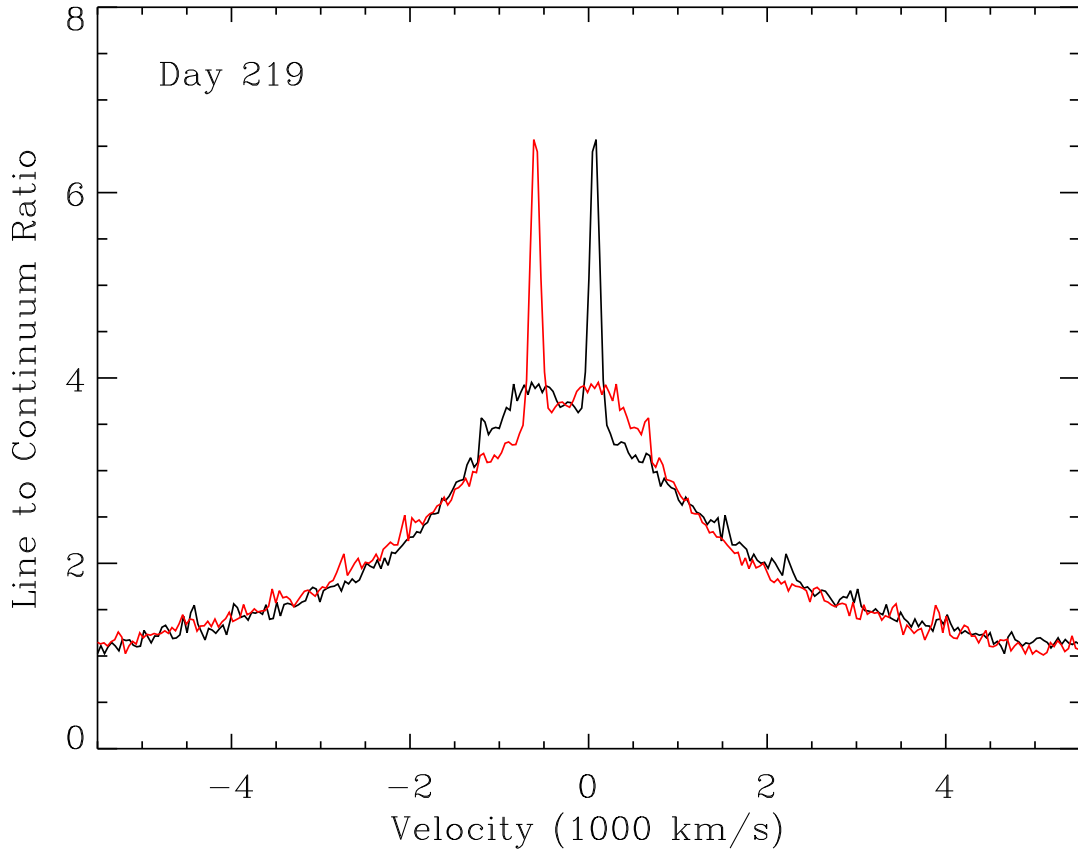


Fig. 6.— Mirroring the profile of Paschen β on day 219 about a velocity of 265 km s^{-1} reveals an asymmetry in the line core when the reflection of the wings is well matched.

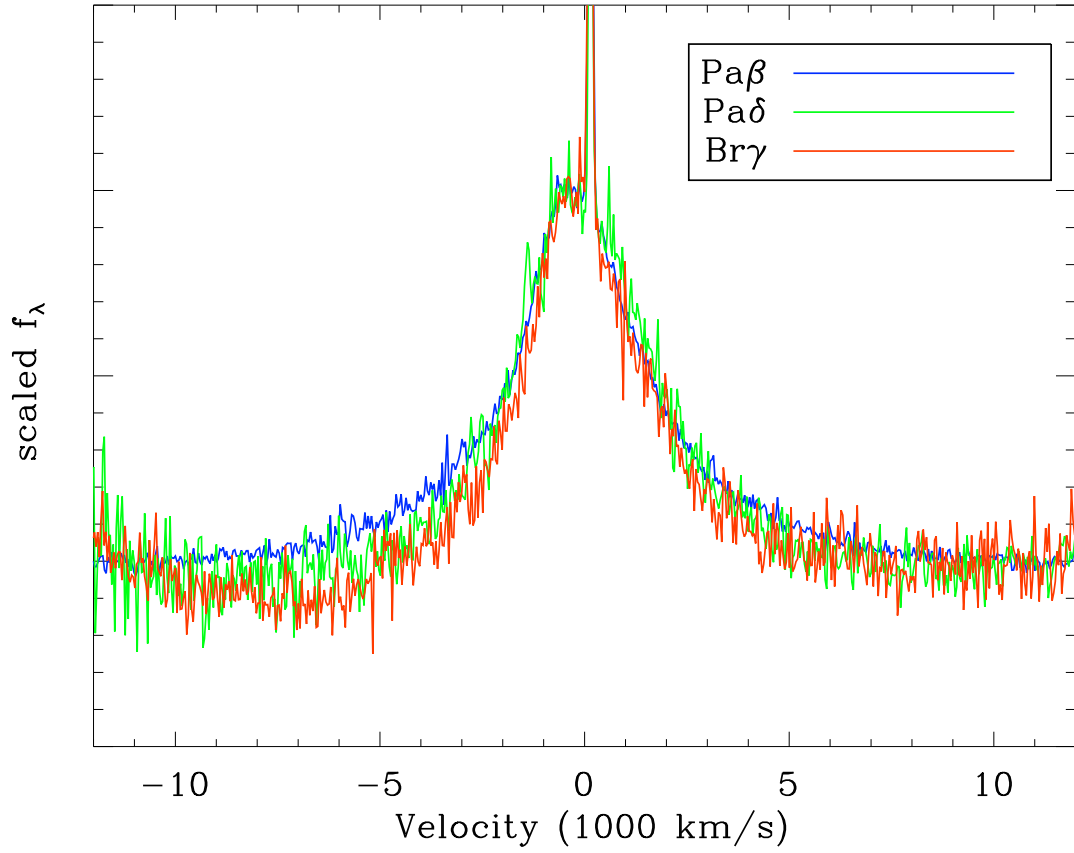


Fig. 7.— Comparison of the different H lines at day 164. After subtraction of a 4865 K black-body, a linear background was fit between velocities of $\pm 10,000 \text{ km s}^{-1}$ and $\pm 12,000 \text{ km s}^{-1}$ and subtracted. Each line was then scaled to a height of 1.

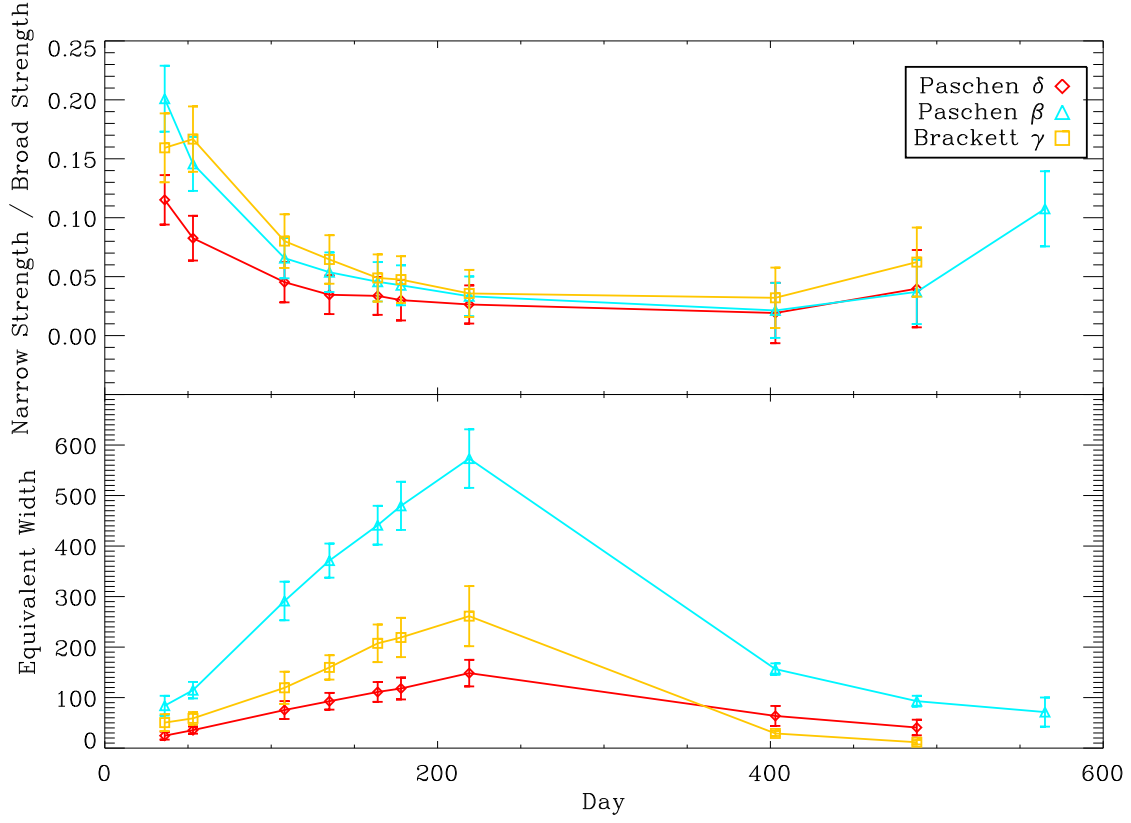


Fig. 8.— Evolution of the equivalent widths and narrow to broad line strengths of several prominent lines. **The equivalent widths plotted include both narrow and broad line flux.**

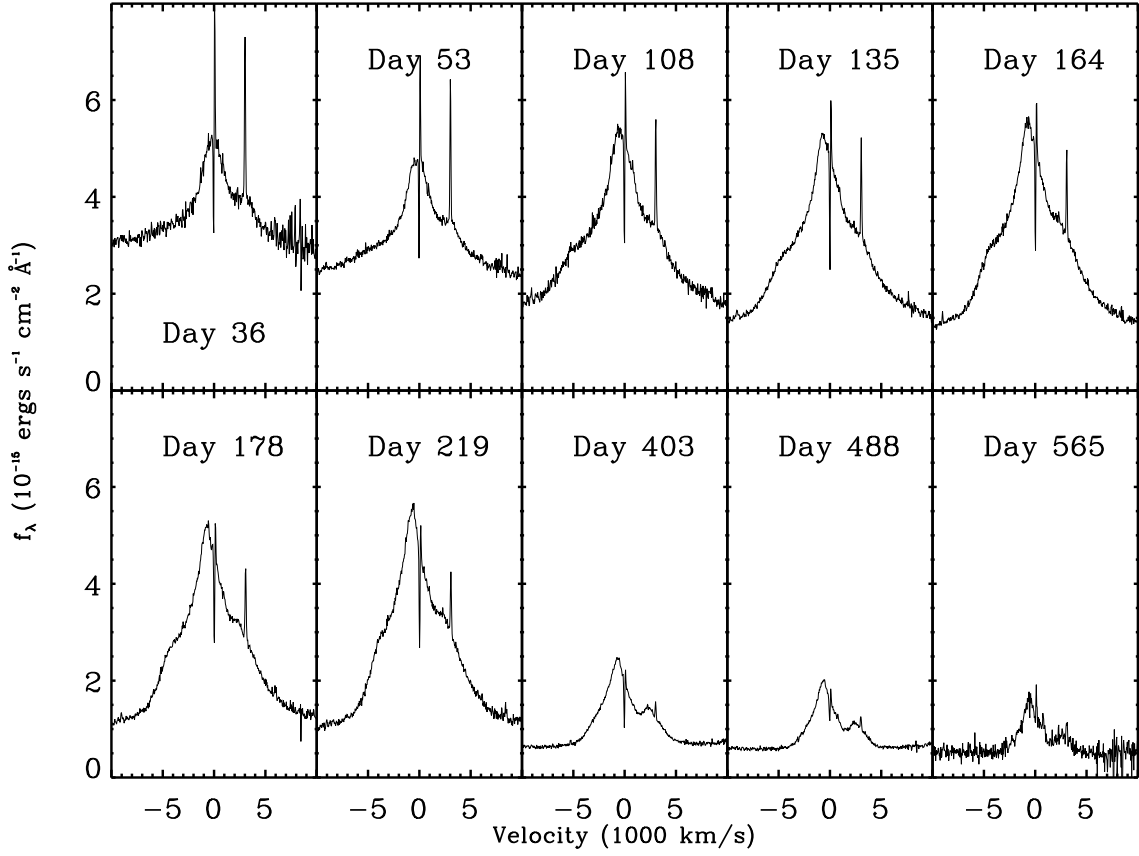


Fig. 9.— Time evolution of the He I $\lambda 10830$ line. The Pa γ line is superposed on the redshifted He I emission.

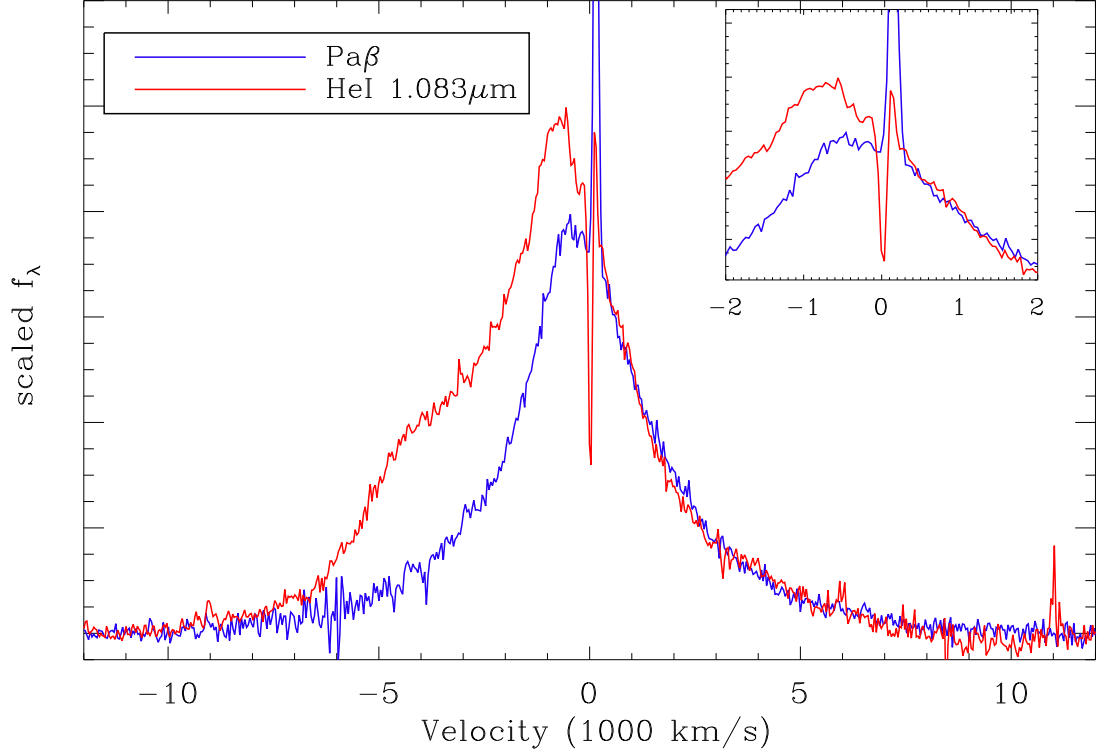


Fig. 10.— Comparison of the He λ 10830 to the H Pa β line at day 178. After subtraction of a 4865 K blackbody, the Paschen β profile was scaled to the strength of the Paschen γ and subtracted, as described in the text. The inset shows the difference in velocity between the peak of the helium profile and that of the hydrogen profile.

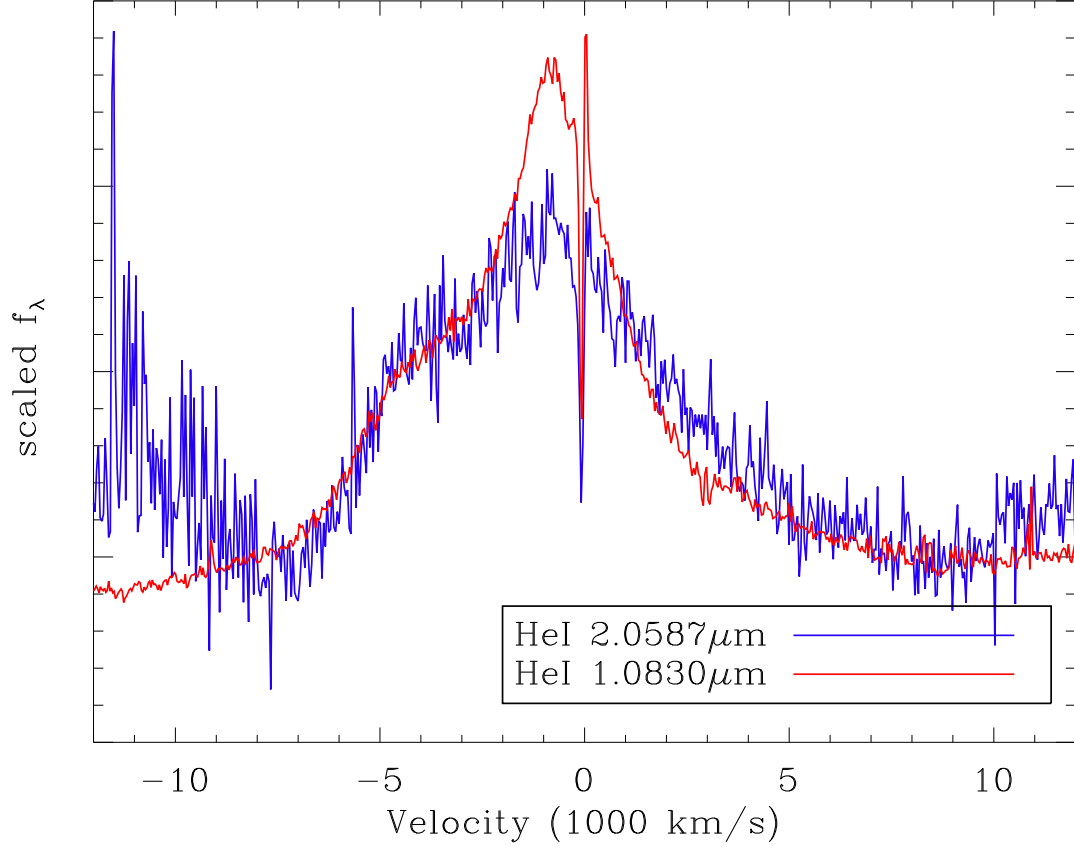


Fig. 11.— Comparison of the He I $\lambda 10830$ line to the $\lambda 20587$ line at day 164. After subtraction of a 4865 K blackbody, a linear background was fitted between velocities of $\pm 7,000 \text{ km s}^{-1}$ and $\pm 9,000 \text{ km s}^{-1}$ and subtracted. Each line was then scaled to a height of 1.

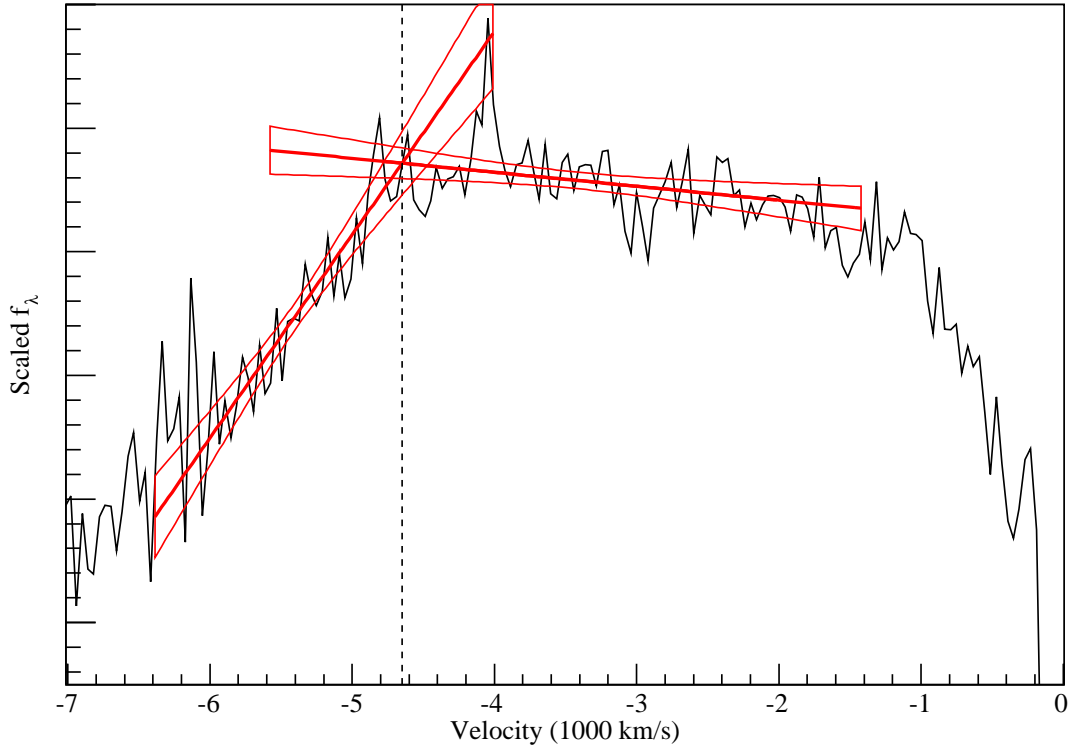


Fig. 12.— The residual of a subtraction of Paschen β from He $\lambda 10830$ (Figure 10), showing the distribution of blueshifted excess He emission on day 178. We find the velocity of the inflection point in the emission (at $\sim -5000 \text{ km s}^{-1}$) by fitting lines to each region adjacent to the inflection point. Also overplotted are regions of 95% confidence about the linear fits. The quoted uncertainty in the inflection point is given by the width of the overlap of the uncertainty regions of each fit.

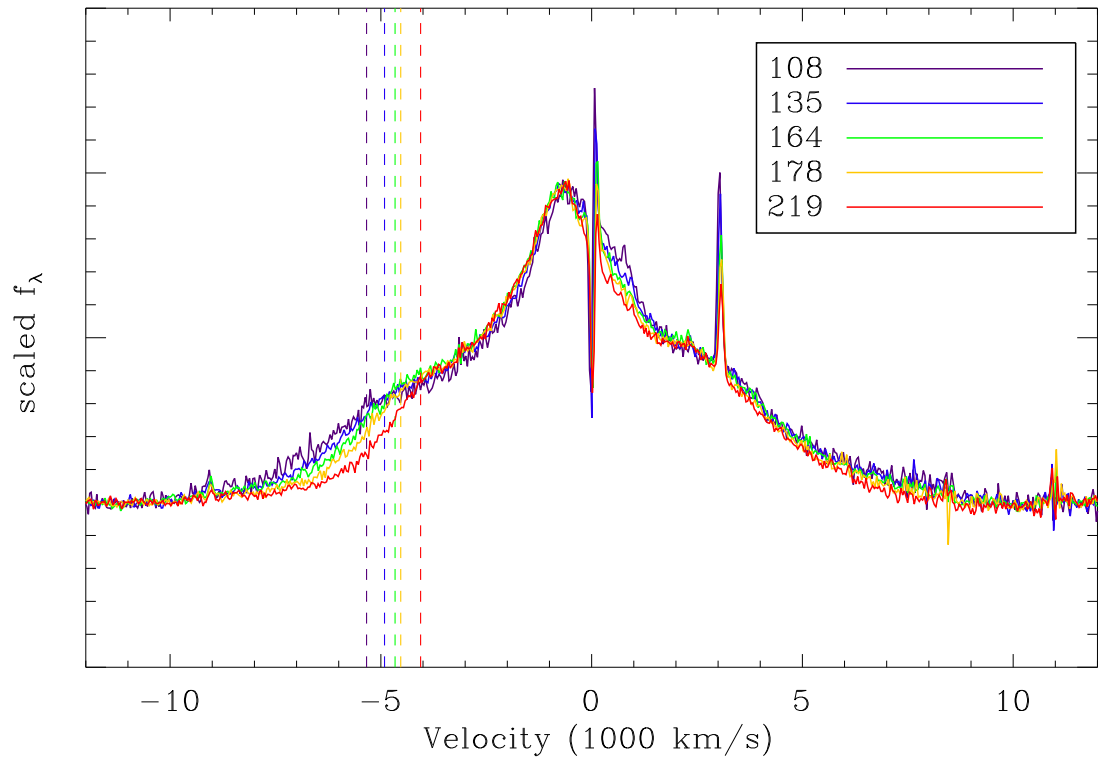


Fig. 13.— Plot of broad He I $\lambda 10830$ emission from day 108 – 219 showing evolution of the broad shoulder. Dashed lines show the velocity of the break in the shoulder at each time.

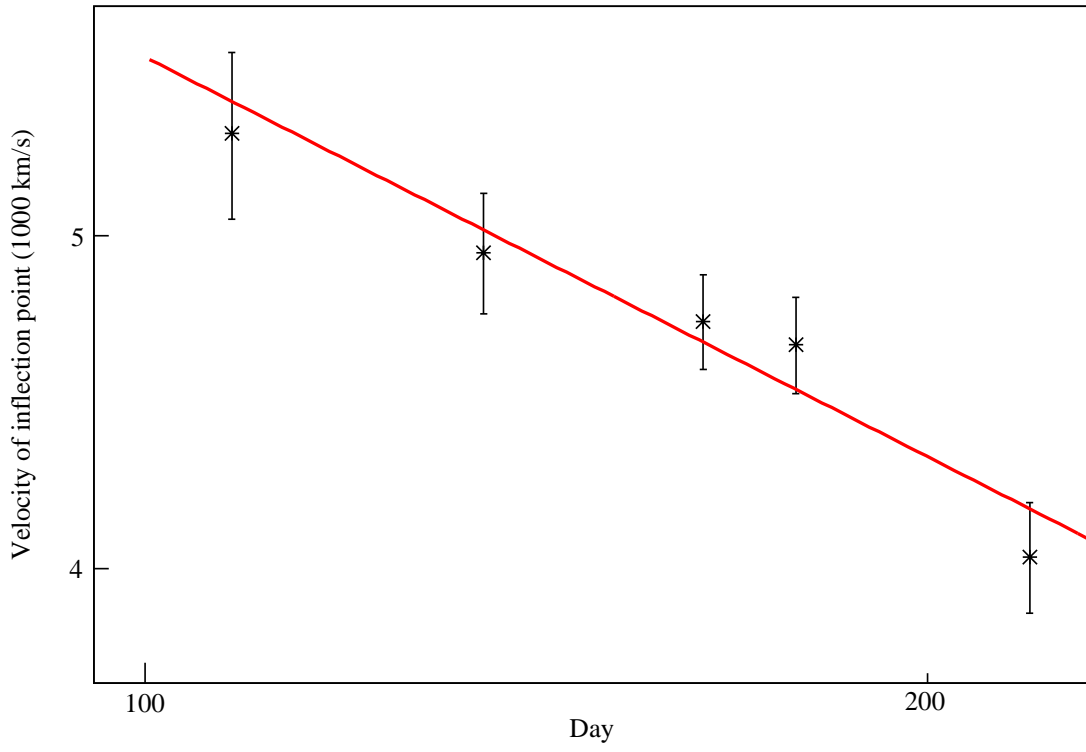


Fig. 14.— Evolution of the velocity of the inflection point in the broad He I $\lambda 10830$ emission profile over days 108–219. This is a log – log plot and the line shows an evolution of velocity $\propto t^{-0.39}$. Error bars have been calculated based on the uncertainty shown in figure 12.

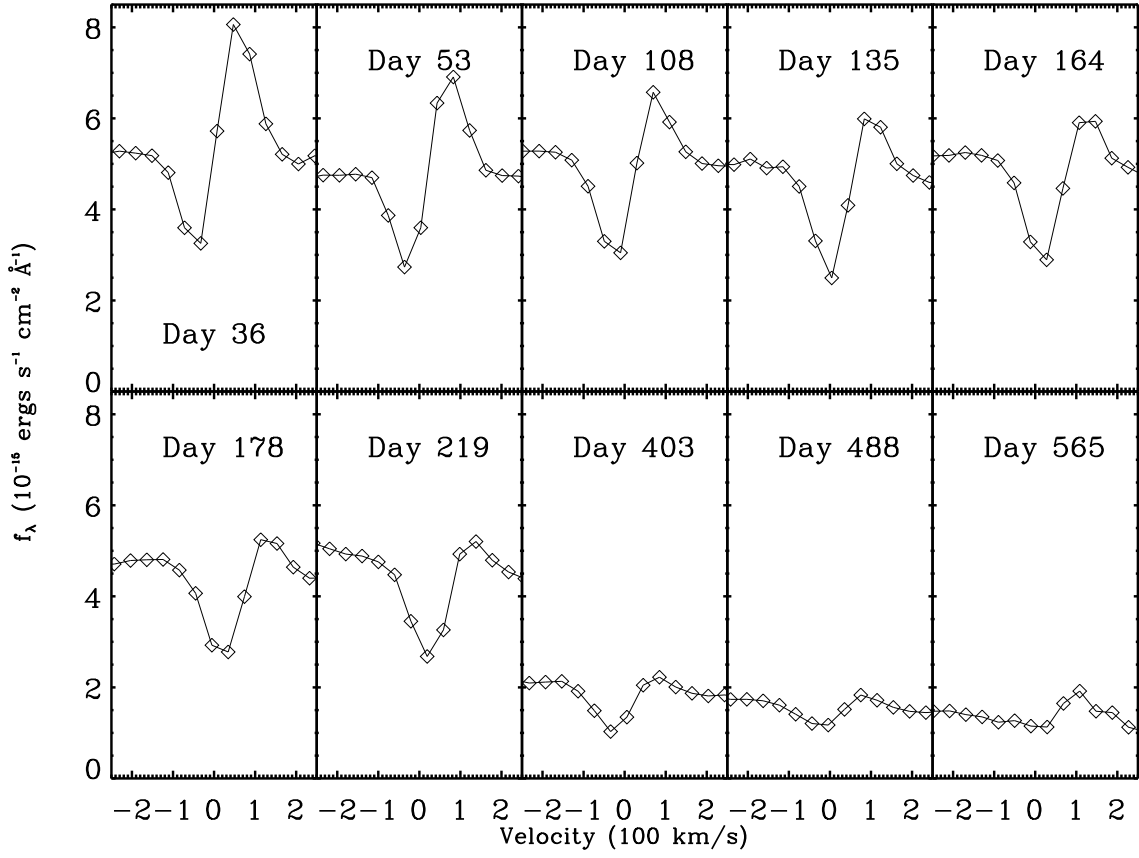


Fig. 15.— Time evolution of the narrow P-Cygni feature in the He I $\lambda 10830$ line.

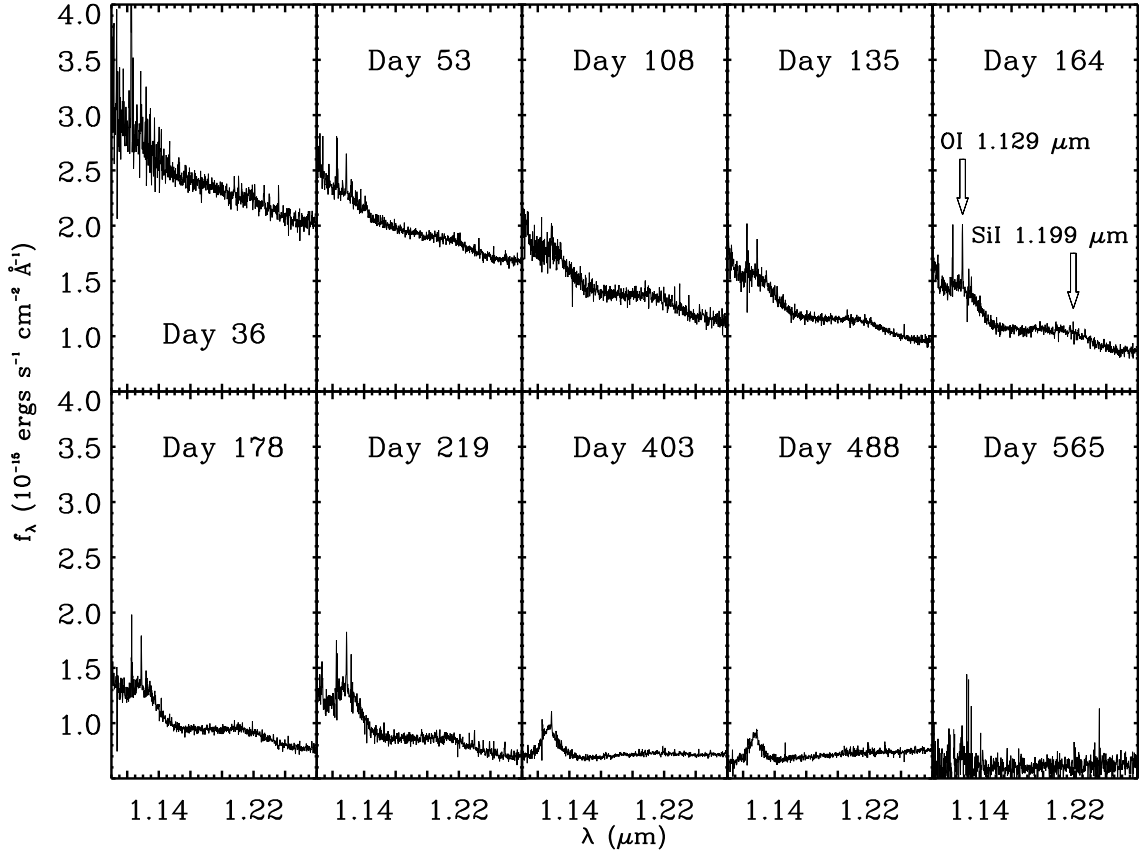


Fig. 16.— Time evolution of the O I $\lambda 11287$ and Si I $\lambda 11991$ features.

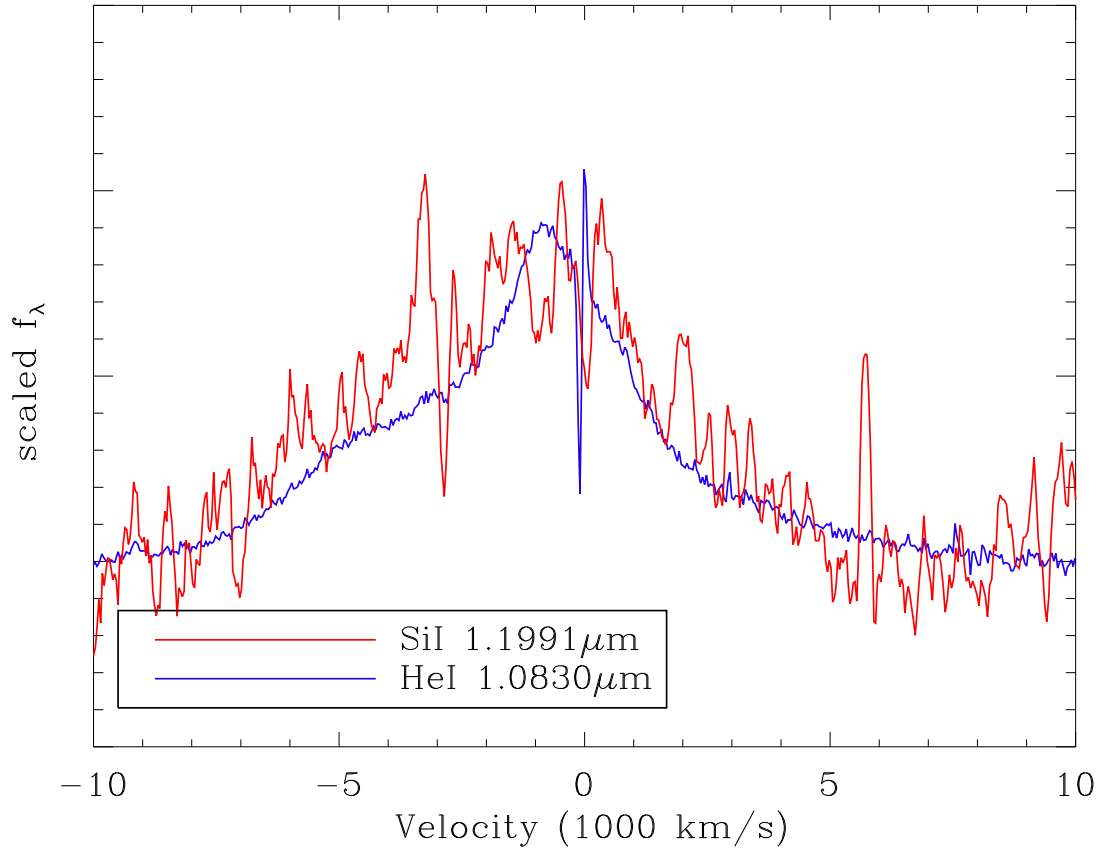


Fig. 17.— Si I $\lambda 11991$ overlaid with He I $\lambda 10830$ on day 135.

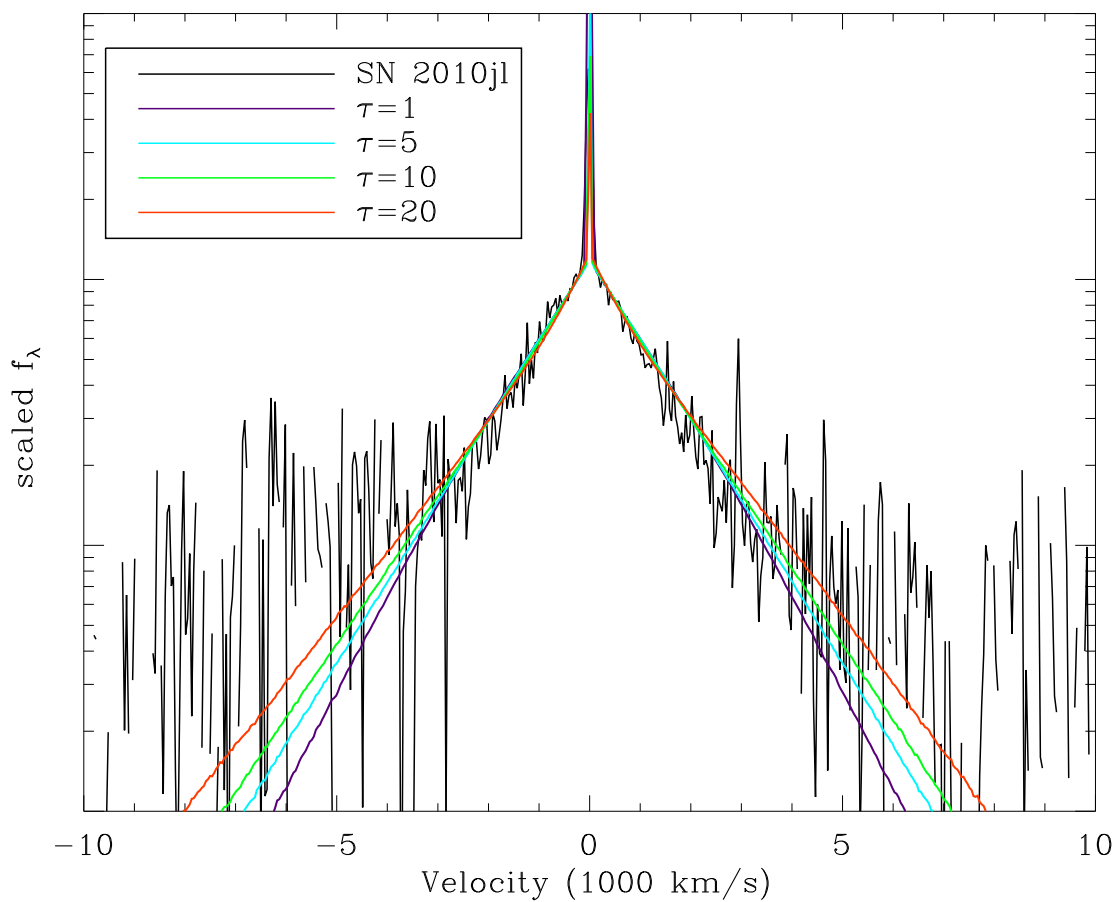


Fig. 18.— Electron scattering profiles overlaid on the broad component of the Paschen β line at an age of 36 days. In order to compare the line profile shapes, the model profiles have been scaled to approximately the same FWHM as the Paschen β line.